Measuring structural nonstationarity: The use of imaging information to quantify homogeneity and inhomogeneity

Efim V. Lavrukhin

Schmidt Institute of Physics of the Earth of Russian Academy of Sciences, Moscow 123242, Russia;
Computational Mathematics and Cybernetics, Lomonosov Moscow State University, Moscow 119991, Russia;
and Dokuchaev Soil Science Institute, Moscow 119017, Russia

Marina V. Karsanina and Kirill M. Gerke ⬤

Schmidt Institute of Physics of the Earth of Russian Academy of Sciences, Moscow 123242, Russia

Heterogeneity is the concept we encounter in numerous research areas and everyday life. While "not mixing apples and oranges" is easy to grasp, a more quantitative approach to such segregation is not always readily available. Consider the problem from a different angle: To what extent does one have to make apples more orange and oranges more "apple-shaped" to put them into the same basket (according to their appearance alone)? This question highlights the central problem of the blurred interface between heterogeneous and homogeneous, which also depends on the metrics used for its identification. This work uncovers the physics of structural stationarity quantification, based on correlation functions (CFs) and clustering based on CFs different between image subregions. By applying the methodology to a wide variety of synthetic and real images of binary porous media, we confirmed computationally that only periodically unit-celled structures and images produced by stationary processes with resolutions close to infinity are strictly stationary. Natural structures without recurring unit cells are only weakly stationary. We established a physically meaningful definition for these stationarity types and their distinction from nonstationarity. In addition, the importance of information content of the chosen metrics is highlighted and discussed. We believe the methodology as proposed in this contribution will find its way into numerous research areas dealing with materials, structures, and measurements and modeling based on structural imaging information.

I. INTRODUCTION

To know if a structure (of the material) at hand is homogeneous or not is necessary to evaluate its physical properties. Examples of such structures are ubiquitous and span from star and galaxy formations [1,2] to nanoporous media [3,4]. The structure of the material defines its major physical properties [5–7] that are usually some averaged fields that allow performing homogenization—in other words, to describe the continuum-scale property as opposed to local field fluctuations due to local structural inhomogeneities (see Table 1.1 in Ref. [5]). In this context, homogeneity equals statistical stationarity. The inhomogeneity poses numerous challenges in different grand research and practical areas: the crystallography studies [8–11]; porous media upscaling [12–15]; CO_2 sequestration into geological formations [16,17]; improving soil fertility [18] or hydrocarbon extraction [19]; evaluating water resources replenishment or contamination hazards [20–22]; global data analysis in geophysics [23]. This list just scratches the surface. Depending on the scale of the structure, different imaging methods are necessary to obtain structural information. For the majority of the problem examples listed above, two imaging methods are utilized to obtain images with resolutions ranging from cm to nm: x-ray

tomography (XCT) and scanning electron microscopy (SEM) [24,25].

To quantify the heterogeneity, we first recall the rigorous definition of the spatial statistical homogeneity and stationarity, which according to the seminal book of Torquato [5], reads as follows: "The media is statistically homogeneous if the joint probability distributions describing the stochastic process are translationally invariant, i.e., invariant under a translation (shift) of the space origin." Or put simpler for inhomogeneity case: "for which the probability density function of any property and its various statistical moments vary spatially, when shifted in space." As applied to images of porous media (as considered in this work), such media are also referred to as macroscopically heterogeneous media, because there is no representative volume element (REV) such that if the media's properties are averaged over such a volume, they will not change if measured in larger volumes or length scales.

Spatial correlation functions (CFs) are powerful structure descriptors immediately available as such joint probabilities or structure descriptors (an example how simpler scalar metrics fail as structural descriptors will be presented later). They are utilized in a multitude of research areas: statistical physics and material sciences [26–28], material design [29,30], rock physics [31–33], soil science [34,35], food engineering [36],

to name a few. Some CFs can be obtained experimentally from *in situ* measurements, such as x-ray tomography [37], nuclear magnetic resonance [38], and small-angle x-ray or neutron scattering (SAXS/SANS) [39]. Known correlation functions allow to perform stochastic reconstructions [40–43] to solve the inverse problem of structure retrieval or multiscale image fusion [44–46]. Measuring CFs or utilizing them for reconstructions usually implies structural stationarity [47,48]. This poses difficulties if the structure possesses significant inhomogeneities [36,49] and requires separate reconstruction treatment for each inhomogeneity region [50]. To finally unlock this Möbius strip of interdependencies between structural measurements such as small-angle scattering [51], measuring and upscaling physical properties [14], and multiscale hierarchy in numerous natural (porous) materials [52], one needs a robust way to measure structural nonstationarity from images.

Abovementioned definitions of the spatially homogeneous media relates to a statistical process rather than its samples that we obtain as digital images. This makes the application of such a definition hardly applicable without imposing additional structural conditions on the data generating process. In most cases of real imaging data this is not possible, unless some well-known sampling procedure is utilized, e.g., Gaussian random field or a regular sphere packing generation. Moreover, it is possible for stationary process to produce "nonstationary" structures [53] due to nonrepresentativeness. In most cases the information about the structure at hand is received using some imaging technology in the form of 2D or 3D images. While for some images it is immediately evident to the naked eye that the structure at hand is nonstationary, in other cases it is not immediately evident. From the viewpoint of classical statistics, to establish stationarity one needs to fit the statistical model of the process for a given image first. Lantuejoul [53] also noted on this problem: "The difficulty in estimating a stereological parameter lies in the fact that such a parameter is a characteristic of a model, and we have only experimental measurements obtained from samples." Establishing the model for given structural image is usually impossible except for some very simple cases. For these reasons, we shall apply terms "stationary" or "statistically homogeneous" to images in the sense of their homogeneity— statistical similarity of subregions. We shall study only the cases where stationarity or nonstationarity is obvious, similar to reconstruction studies based on Gaussian random fields [54–56], multiple-point statistics [50] and simulated annealing [23]. The considerations above highlight the lack of a physically sound criterion based on theoretical considerations that could be used instead of the strict definition above for the digital image analysis.

In this paper, we propose a methodology to quantify heterogeneity and reveal the blurry boundary between stationary and nonstationary structures based on imaging data. Using porous media images, with the help of CFs computation and clustering, we establish a way to divide the image into zones with similar structures. Thus, our work is based on the following assumptions:

(1) We analyze the (in)homogeneity of the image on a predetermined scale D. The answer to this problem may differ depending on the chosen scale D (see size of the patch below);

(2) We assume that some small portion of the image (a patch of size D) is homogeneous, i.e., it is possible to average the statistical characteristics inside it (and compute CFs to describe the structure);

(3) Homogeneous subregions consist of a set of connected patches. Subregions can belong to the same homogeneity cluster but are not connected to each other;

(4) We propose (in)homogeneity conditions for a given image based on the structural information presented in image itself without using any *a priori* statistical assumptions.

Below we first describe the details of our methodology and, with real images, demonstrate how it helps to assess structural nonstationarity. Next, we show some important results and provide evidence that some particular structures are stationary. Based on these results, we discuss some important immediate outcomes relevant to the structure and physical properties measurements, stochastic reconstructions, and representativeness. Summarily we highlight the most important applications and the outlook of potential usage to quantify and compare different structures.

II. METHODS

For ease of explanations we shall consider only 2D images, keeping in mind that extension to 3D is straightforward. We start from a description of major building blocks of the methodology, and then describe each step of the algorithm in detail. On the upper level, our methodology for determining (in)homogeneity is based on solving the clustering problem and consists of the following steps:

(1) Split the input image into a grid of overlapping square 2D image patches of a given size D;

(2) For each 2D image patch calculate its vector representation (the name "vector descriptor" is also used in the text) based on the given set of correlation functions;

(3) Divide the set of obtained 2D image patches into separate clusters based on pairwise $\mathcal{L}_2$ distances between their vector representations;

(4) Determine if the resulting clustering is significant based on the two following criteria:

1. The distribution of $\mathcal{L}_1$ distances between whole image and 2D patches in vector representation space;

2. A pairwise $\mathcal{L}_1$ distances between obtained clusters centers (also in vector representation space).

A. Patches grid

In this subsection, we will consider in detail the algorithm for constructing a grid of overlapping patches on the original image.

The first parameter of patches' grid is D — this is the number of the pixels on each side of the square patch. Subregions consist of a connected set of patches. To make the borders of the subregions smoother, it is convenient to let the patches intersect with each other. To describe such intersections, we introduce one more parameter of the algorithm: O (overlay)— this is the number of pixels by which the patches adjacent to the grid are overlapped. For a grid with the specified properties to be constructed correctly, the following conditions for
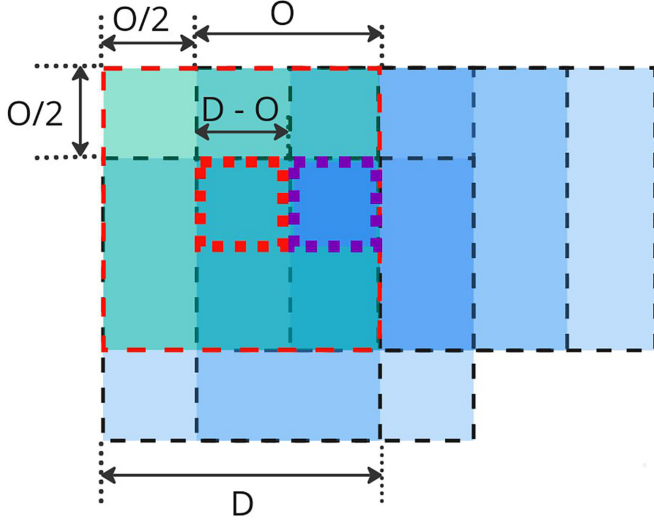
FIG. 1. An example of building a coordinate grid using the proposed algorithm. Here we consider the top left corner of the image grid. The selected patch is highlighted in red dotted line and green color. The red thick line highlights the subpatch corresponding to the given patch. The thick purple line shows the subpatch corresponding to the next patch on the right of the current one. The method assigns a cluster label only for the subpatch based on the feature representation vector p_{ij} calculated over the entire patch. Other patches that are under consideration are highlighted in blue. The image also shows the size of patch D, the subpatch of size $D - O$; patches overlap by O pixels, and the size of the unlabeled image frame $\frac{O}{2}$ that will not be clustered after applying the methodology. In the depicted example $O = \frac{D}{3}$.

aforementioned parameters must be met:

$$\begin{cases} D \mod (D - O) = 0, \\ \frac{O}{D-O} \mod 2 = 0. \end{cases} \tag{1}$$

In this case the membership of the whole patch to the cluster defines the cluster label only for the central subpatch of size $(D - O) \times (D - O)$, because each pixel from the central subpatch belongs to the center of exactly one patch (see Fig. 1 for details).

It is convenient to make the size of the intersection of the patches depend on the size of the patches themselves. After a number of experiments, we adopted the parameter value of $O = \frac{4D}{5}$.

Summarizing the advantage of the above organization of a grid of intersecting patches, we highlight following points:

1. Better boundaries' smoothness for selected homogeneous subregions;

2. A cluster label is uniquely defined for each pixel of the input image;

3. Clustering of the central subpatch is more symmetrical. In other words, it takes into account the contribution of less distant pixels into the vector representation p_{ij} of the patch m_{ij} [see Eq. (4)], i.e., pixels at a distance of no more than $\frac{\sqrt{2}D}{2}$ contribute to the vector representation for the pixels of the center subpatch, as opposed to the case $O = 0$ where the label of the top left pixel of the patch is affected by the lower right pixel at a distance of $\sqrt{2}D$.

Now consider the restrictions on the possible sizes of the input image as imposed by the patch size. An image of size $H \times W$ can be fragmented into (assuming $H > D$ and $W > D$) K_H patches in height and K_W in width:

$$K_H = \left\lfloor \frac{H - D}{D - O} \right\rfloor + 1,$$

$$K_W = \left\lfloor \frac{W - D}{D - O} \right\rfloor + 1,$$

$$\tilde{H} = O + K_H \times (D - O),$$

$$\tilde{W} = O + K_W \times (D - O). \tag{2}$$

Thus, we will not be able to determine in advance the clusters for pixels that do not fit into the outer patches (lying outside the cropped image of size $\tilde{H} \times \tilde{W}$). Also, around the image with dimensions of $\tilde{H} \times \tilde{W}$ there will be a nonsegmented frame that is $\frac{O}{2}$ wide, this frame size is highlighted in Fig. 1 [evenness of O follows from Eq. (1)].

As a simple solution, we crop the image to the desired dimensions of $\tilde{H} \times \tilde{W}$ and do not consider pixels outside the frame of size $\frac{O}{2}$, so the output image has dimensions of $(\tilde{H} - O) \times (\tilde{W} - O)$ pixels. Alternatively, one could do exactly the opposite—complement the image using mirroring in such a way that a cluster can be set for each pixel of the original image, but this solution would result in some artifacts at the edges.

B. Calculation of the structural descriptors

Suppose we have an image M of size $H \times W$, we denote the operation of extracting a pixel at coordinates (x, y) as $M[x, y]$. To sample "joint probabilities," we compute correlation functions for the whole image (and also for its 2D or 1D patches): two-point probability S_2 and lineal L_2 for the pore phase within a square region. These functions describe the probability that two points separated by a line segment lie in the same phase and the probability that the whole segment lies within the same phase, correspondingly. Correlation functions are computed along two major orthogonal directions [57,58] with a correlation length of $L_{\max} = \frac{D}{2}$ and then stacked into a single vector Eq. (4). In the case of 2D images, correlation functions of the entire image M using the maximum correlation length parameter $L_{\max}$ can be written as follows:

$$S_2^x[r|M] = \frac{\sum_{x,y} I[M[x, y] = M[x + r, y] = 1]}{W(H - r)},$$

$$S_2^y[r|M] = \frac{\sum_{x,y} I[M[x, y] = M[x, y + r] = 1]}{(W - r)H},$$

$$L_2^x[r|M] = \frac{\sum_{x,y} I[M[x, y] = \dots = M[x + r, y] = 1]}{W(H - r)},$$

$$L_2^y[r|M] = \frac{\sum_{x,y} I[M[x, y] = \dots = M[x, y + r] = 1]}{(W - r)H}, \tag{3}$$

where $I[\cdot]$ is pixel indicator function, x and y defines the direction of function calculation, $r < L_{\max}$. $L_{\max}$ can be as large as image dimensions, but with larger r the number of samples decreases and usually leads to somewhat noisy tails (e.g., see correlation functions in work [35]), so we used $L_{\max} = \frac{D}{2}$ in out study.

Let us denote vector representation V of our images and patches as concatenation of correlation functions vectors that now can be computed as

$$V^x(m) = \left[S_2^x[\cdot|m], L_2^x[\cdot|m]\right],$$
$$V^y(m) = \left[S_2^y[\cdot|m], L_2^y[\cdot|m]\right],$$
$$V(m) = [V^x(m), V^y(m)]. \tag{4}$$

Next, we use directional correlation functions descriptors V^d for the vector representation of one-dimensional patch $m_{i,j}^d$ and concatenated descriptors V of two-dimensional patches $m_{i,j}$, as well as the entire image M, where i, j are the coordinates of patch's upper-left pixel in rectangular grid of original image M, d is the direction of the 1D patch.

In general, to apply our method, we compute the following feature representations:

1. for the whole image M as $P = V(M)$;
2. for each 2D image patch $m_{i,j}$ as $p_{i,j} = V(m_{i,j})$;
3. for each 1D image patch $m_{i,j}^d$ as $l_{i,j}^d = V(m_{i,j}^d)$ for $d \in \{x, y\}$.

Note that 1D patch has $(D, 1)$ shape for $d = x$, and $(1, D)$ shape for $d = y$, 2D patch has (D, D) shape, whole image has (H, W) shape—but all such objects has the same vector descriptors shape for a given direction: V^d consists of $2L_{\max}$ elements for each direction d [and $4L_{\max}$ for whole V vector-descriptor, but it can be computed only for source image and 2D patches, see Eq. (4)].

C. Distance function

In our method we use the standard $\mathcal{L}_2$ metric defined as

$$\mathcal{L}_2(v_1, v_2) = ||v_1 - v_2||_2 = \sqrt{\sum_{i=1}^{N}(v_1[i] - v_2[i])^2}. \tag{5}$$

We used averaged $\mathcal{L}_1$-metric as distance measure:

$$\mathcal{L}_1^{\text{avg}}(v_1, v_2) = \frac{\sum_{i=1}^{N}|v_1[i] - v_2[i]|}{N} = N||v_1 - v_2||_1. \tag{6}$$

We introduce linear distance between 2D patches a and b as

$$d(a, b) = \mathcal{L}_1^{\text{avg}}(V(a), V(b))$$
$$= \frac{||V(a) - V(b)||_1}{4L_{\max}}$$
$$= \frac{||V^x(a) - V^x(b)||_1}{2L_{\max}} + \frac{||V^y(a) - V^y(b)||_1}{2L_{\max}}$$
$$= \mathcal{L}_1^{\text{avg}}(V^x(a), V^x(b)) + \mathcal{L}_1^{\text{avg}}(V^y(a), V^y(b))$$
$$= d^x(a, b) + d^y(a, b). \tag{7}$$

In this case, linearity means that we can compute the distance along the axes separately, that is, the distance along the full vector representation $V(\cdot)$ is equal to the sum of the distances between the vector representations along the individual axes $V^x(\cdot)$ and $V^y(\cdot)$. This fact allows us to calculate the distance between 1D and 2D patches along any axis for which the 1D patch is specified. This property will be useful for thresholds calculation in Eq. (11).
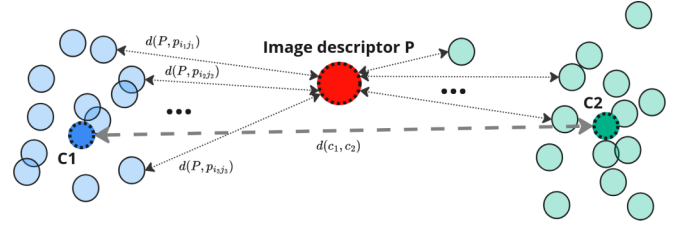

FIG. 2. Visualization of the proposed homogeneity conditions in a descriptor vectors space projected to coordinate plane using PCA method. In fact, the descriptors space has size $4L_{\max}$, so coordinate plane is used for ease of perception. Large red dot is the image descriptor P, small blue and green dots are 2D patches from two different clusters, the circled bright dots are the centers of the clusters. Note that clustering (division of points into green and blue groups) is done in descriptors space based on the $\mathcal{L}_2$ distance by Eq. (5). Arrows represent distances and are calculated in descriptors space based on the $\mathcal{L}_1$ distance in Eq. (7). The distances between the image descriptor P and all other patches $p_{i,j}$ are highlighted by black dotted arrows and refer to the condition in Eq. (9), while the distance between c_1 and c_2 clusters is highlighted by gray dashed arrow and refers to condition in Eq. (10).

D. Clustering

After descriptor vectors calculation we carry out clustering of image patches in the space of their vector representations $p_{i,j}$. For this we use K-Means clustering, that constructs spherical clusters based on $\mathcal{L}_2$ distance function in Eq. (5) (this is the only place in the proposed methodology where it is necessary to use exactly $\mathcal{L}_2$ metric). For (non)homogeneity analysis we use only the clustering into two clusters (but it is possible to use any number of clusters as will be demonstrated later for separation of images into heterogeneous zones). After the clustering procedure we can assign a class label for each subpatch from the entire set of subpatches and, thus, get the coloring of the entire image into homogeneous subregions (see clustering examples on Fig. 7)

Also, at this stage we can obtain a set of cluster center vectors in descriptors space: $\{c_i\}_{i=1}^{K}$, $c_i \in \mathbb{R}^{4L_{\max}}$ (as mentioned earlier, in a common case of (in)homogenity analysis $K = 2$). The clusters' centers will be used in the subsequent method steps.

E. Homogeneity conditions

The final step of the methodology is to determine if the image is homogeneous. To do this, we compute distribution of distances [according to Eq. (7)] between full image descriptor P and descriptors of 2D patches $p_{i,j}$ as

$$F(x) = \mathbb{P}(d(P, p) \leqslant x), \tag{8}$$

where the distribution is calculated over the entire set of patches and x is the considered distance in descriptors space. You can see an example of such distribution histogram at the bottom of the Fig. 3.

Based on this distribution, we introduce following homogeneity condition:

$$\mathbb{H}_{\text{homo}}(T_{\text{homo}}, \alpha) : F(T_{\text{homo}}) > \alpha. \tag{9}$$
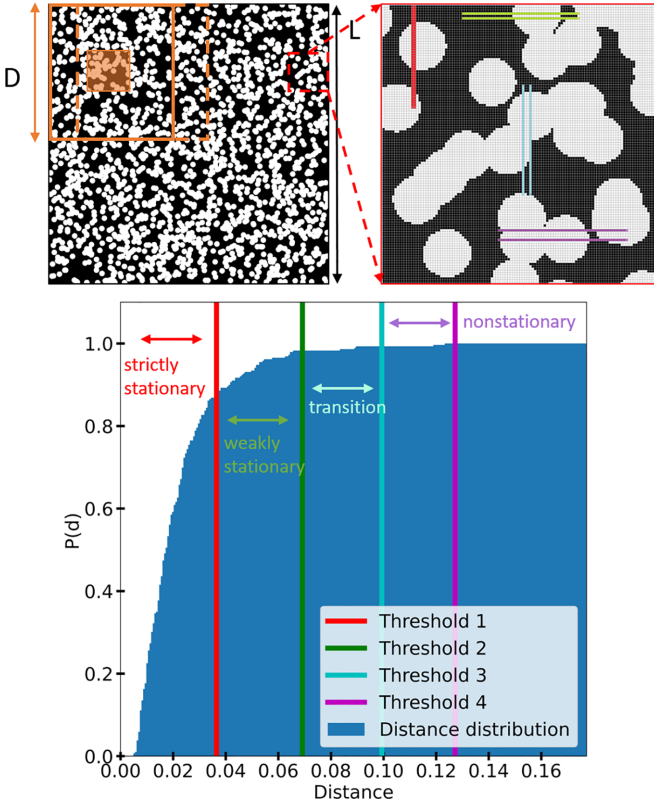
FIG. 3. The graphical explanation of Thresholds, their evaluation from original images, and four stationarity-nonstationarity zones. Red line indicates stationarity T_1, green—weakly stationary T_2, blue—transition T_3, and purple—definitely nonstationary T_4. The upper right zoomed image of Poisson circles shows how thresholds are calculated for different distances. Red slices on 2D image are next to each other (i.e., $r = 1$), green slices are one pixel apart ($r = 2$), blue—two pixels ($r = 3$), and purple—three pixels apart ($r = 4$) [see thresholds values in Eq. (12)]. Such differences between slices are in good agreement with evaluation of artificial and real images for which we are sure if they are purely or weakly stationary or nonstationary at all (see Results section and numerous calculations as presented in the Supplemental Material [59]). The bottom image shows the distance thresholds depicted on the histogram of 2D patch distance distributions from Eq. (8).

This criterion checks what proportion (controlled by parameter α that is something similar to the significance level) of all patches that differ only slightly (controlled by parameter T_{homo}) from the whole image (see black dotted arrows between image descriptor P and all patches representations p in the Fig. 2). In the next subsection, we shall suggest how to establish parameter T_{homo} from the structural information (i.e., from the image itself) and parameter α.

Further, we introduce second homogeneity condition based on distance between clusters (it is applicable even if number of clusters K is greater than 2):

$$\mathbb{H}_{\text{clusters}}(T_{\text{clusters}}) : \exists i, j, \ i \neq j : \ d(c_i, c_j) < T_{\text{clusters}}. \quad (10)$$

The meaning of this condition is quite straightforward: in a homogeneous image, the selected clusters cannot be very far (based on parameter T_{clusters}) from each other (see bold gray dotted arrow between clusters in the Fig. 2). Similar
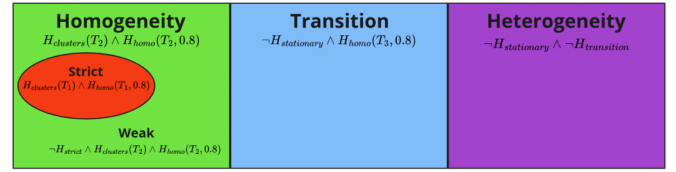

FIG. 4. Visual relationship between image homogeneity classes based on proposed conditions. The class of homogeneous images includes a subclass of strictly homogeneous images, while the other classes do not intersect with each other.

to the previous criterion, we will establish parameter T_{clusters} using the information extracted from the image in the next subsection.

The originality of the proposed approach lies with the fact that we do not pose any *a priori* assumptions about the nature of distance distributions, except for the level of significance α.

F. Threshold evaluation

To get the threshold values, we will construct a function of the $\mathcal{L}_1$ distance between 1D patches in descriptors space from the distance between patches in image coordinates grid.

We estimate $\rho(r)$, where $\rho(r)$ is the mean distance between vector representations of two 1D patches (slices) in the same direction of the coordinate axes and lying at a distance r from each other in coordinates grid of the original image. Function $\rho(r)$ is averaged over distances from Eq. (7), i.e., calculated over all possible 1D patches pairs in the image between feature representations of such 1D slices:

$$
\begin{aligned}
\rho(r) &= \mathbb{E}_{ij} d^x \big(V(m_{i+r,j}^x), V(m_{i,j}^x) \big) \\
&+ \mathbb{E}_{kl} d^y \big(V(m_{k,l+r}^y), V(m_{k,l}^y) \big) \\
&= \mathbb{E}_{ij} d^x \big(l_{i+r,j}^x, l_{i,j}^x \big) + \mathbb{E}_{kl} d^y \big(l_{k,l+r}^y, l_{k,l}^y \big), \quad (11)
\end{aligned}
$$

where $\mathbb{E}_{i,j}$ is mathematical expectation over all possible values of coordinates i and j. You can view the visual examples with one-dimensional patches at different distances in the image grid in Fig. 3. Note that for real images, the function will be monotonic with a gradual plateau. At the same time, it is easy to construct a sample where this is not the case, for example, in the case of strictly periodic images.

Now we can introduce the thresholds evaluation:

$$
\begin{aligned}
T_{\text{clusters}_1} &= T_{\text{homo}_1} = T_1 = \rho(1), \\
T_{\text{clusters}_2} &= T_{\text{homo}_2} = T_2 = \rho(2), \\
T_{\text{clusters}_3} &= T_{\text{homo}_3} = T_3 = \rho(3), \\
T_{\text{homo}_4} &= T_4 = \rho(4). \quad (12)
\end{aligned}
$$

At the previous stage we got the cluster centers with feature vectors of $\{c_i\}_{i=1}^K$. Now we have all necessary information to formulate our semiempirical conditions for the (in)homogeneity image analysis following these steps (see Fig. 4 with the mutual arrangement of classes):

(1) Strictly stationary images: $\alpha_1 = 0.8$,
$$\mathbb{H}_{\text{strictly}} = \mathbb{H}_{\text{homo}}(T_1, \alpha_1) \wedge \mathbb{H}_{\text{clusters}}(T_1)$$
(2) Weakly stationary images: $\alpha_2 = 0.8$,

$$\mathbb{H}_{\text{weakly}} = \neg \mathbb{H}_{\text{strictly}} \wedge (\mathbb{H}_{\text{homo}}(T_2, \alpha_2) \wedge \mathbb{H}_{\text{clusters}}(T_2)),$$
$$\mathbb{H}_{\text{stationary}} = \mathbb{H}_{\text{homo}}(T_2, \alpha_2) \wedge \mathbb{H}_{\text{clusters}}(T_2)$$
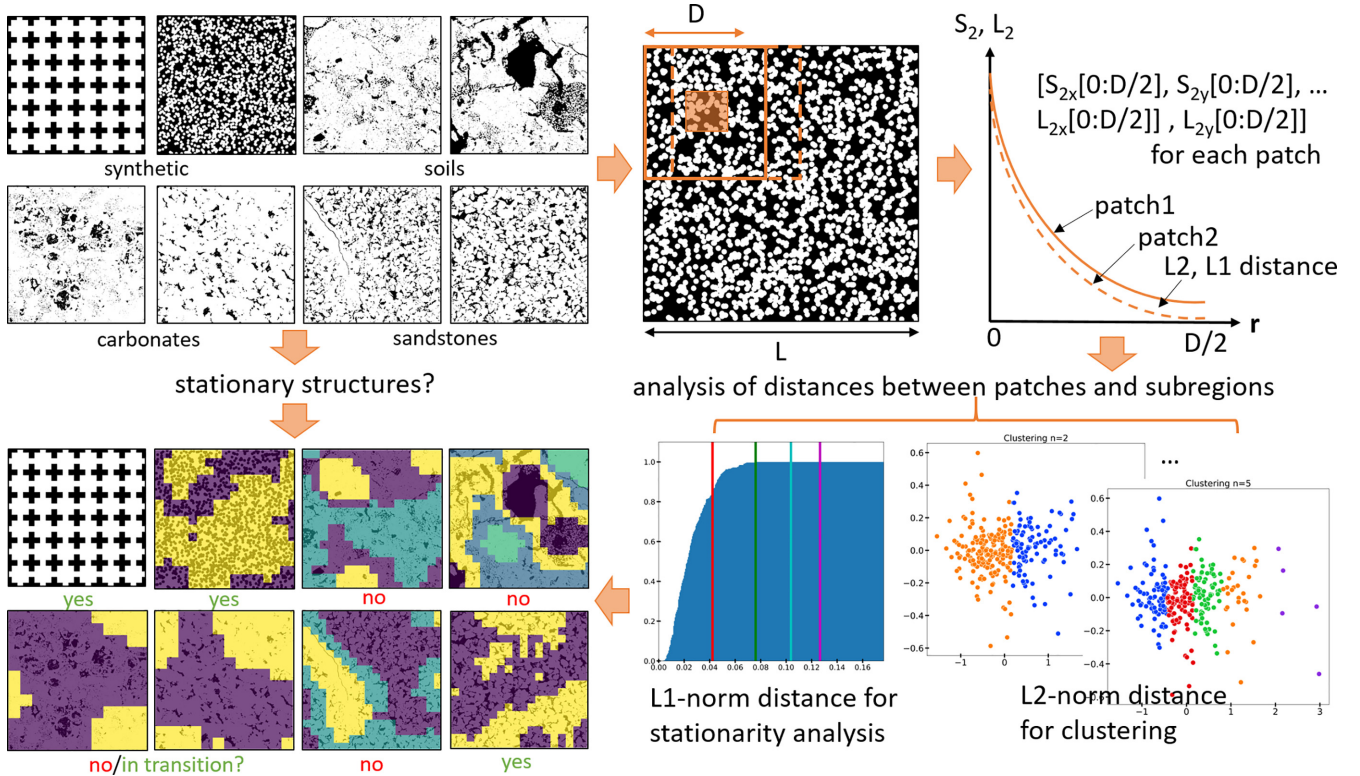
FIG. 5. The general scheme of stationarity quantification with the help of the correlation functions. On the scheme, D refers to the width of the sampling patch in pixels, L is the width of the image, S_2 and L_2 with additional suffixes refer to correlation functions computed in major orthogonal directions. In the upper left corner there are examples of binary 2D images of different homogeneity. In the middle of the upper row, the procedure for bypassing the 2D image with a sliding window is shown with the calculation of correlation functions for a 2D patch of size D. The right picture in the top row shows an example of what the difference between the two vector representations of patches might look like. Since only one correlation function is shown, the graph can be drawn depending on the length of the correlation, in the example the length $L_{max} = \frac{D}{2}$. The x axis plots the length of the correlation, the y axis shows the value of the correlation function. Depending on the task, the distance between vector representations is considered differently: $\mathcal{L}_2$ metric used for clustering and $\mathcal{L}_1$ for (in)homogeneity determination. The right picture in the bottom row shows the function in Eq. (8) (on the left side) and the results of clustering (on the right side). On the distribution histogram, one can see which patches fraction is covered by the distance value equal to one of the four thresholds according to Eq. (12) (threshold colors labels can be seen in Fig. 3). For visualization purposes, the results of K-Means clustering shown on a two-dimension plane (we used only two first components of the PCA decomposition of patches vector representations, raw patches representation vectors has $4L_{max}$ dimensions and, thus, hard to get visualized). The "yes" and "no" marks in left picture in the bottom row highlight the results of our quantification—if a given structure is stationary or not (additional details of the quantification based on distances between clusters are shown in Fig. 3 and Fig. 6). More comprehensive methodological description of image analysis steps presented in Sec. II. Results of clustering for a variety of input images can be found in Ref. [59].

(3) Transition images: $\alpha_3 = 0.8$,
$\mathbb{H}_{transition} = \neg \mathbb{H}_{stationary} \wedge \mathbb{H}_{homo}(T_3, \alpha_3)$
(4) Nonstationary images: $\mathbb{H}_{nonstationary} = \neg \mathbb{H}_{stationary} \wedge \neg \mathbb{H}_{transition}$

III. RESULTS, DISCUSSION, AND OUTLOOK

We start by considering various real and synthetic images of porous media: periodic crosses, Poisson circle packing, sandstones, carbonates, and soils. Experimental images are binary—they consist of the pore and solid phases, as obtained by segmenting XCT or SEM data. Now, following the methodology described in the previous section we analyze these 2D images according to the overall pipeline in Fig. 5.

Based on image analysis only periodic structures (such as crosses on Fig. 5) are stationary according to the strict definition cited above. If we apply our methodology to such

a periodic image, then we observe zero differences between windows placed exactly within the periodic unit cells (thus, not shown), but some nonzero differences are observed in case we do not sample such cells exactly (Fig. 6). The analysis as presented in Fig. 5 reveals that images of natural porous structures are never strictly stationary—this agrees with previous notion that images of laboratory-scale natural porous media, since their porosity distribution follows a fractional Brownian motion, a nonstationary stochastic distribution, should be considered as at least weakly nonstationary [60]. So is the random penetrable circles packing image with limited resolution from Fig. 5, which results from the stationary Poisson random process and should be considered to produce a stationary structure [5]. We argue that such structures are indeed stationary, but we shall refer to them as "weakly" stationary. This "nonstrict stationarity" originates from the digital nature of the imaging procedure (limited imaging resolution [61–63])
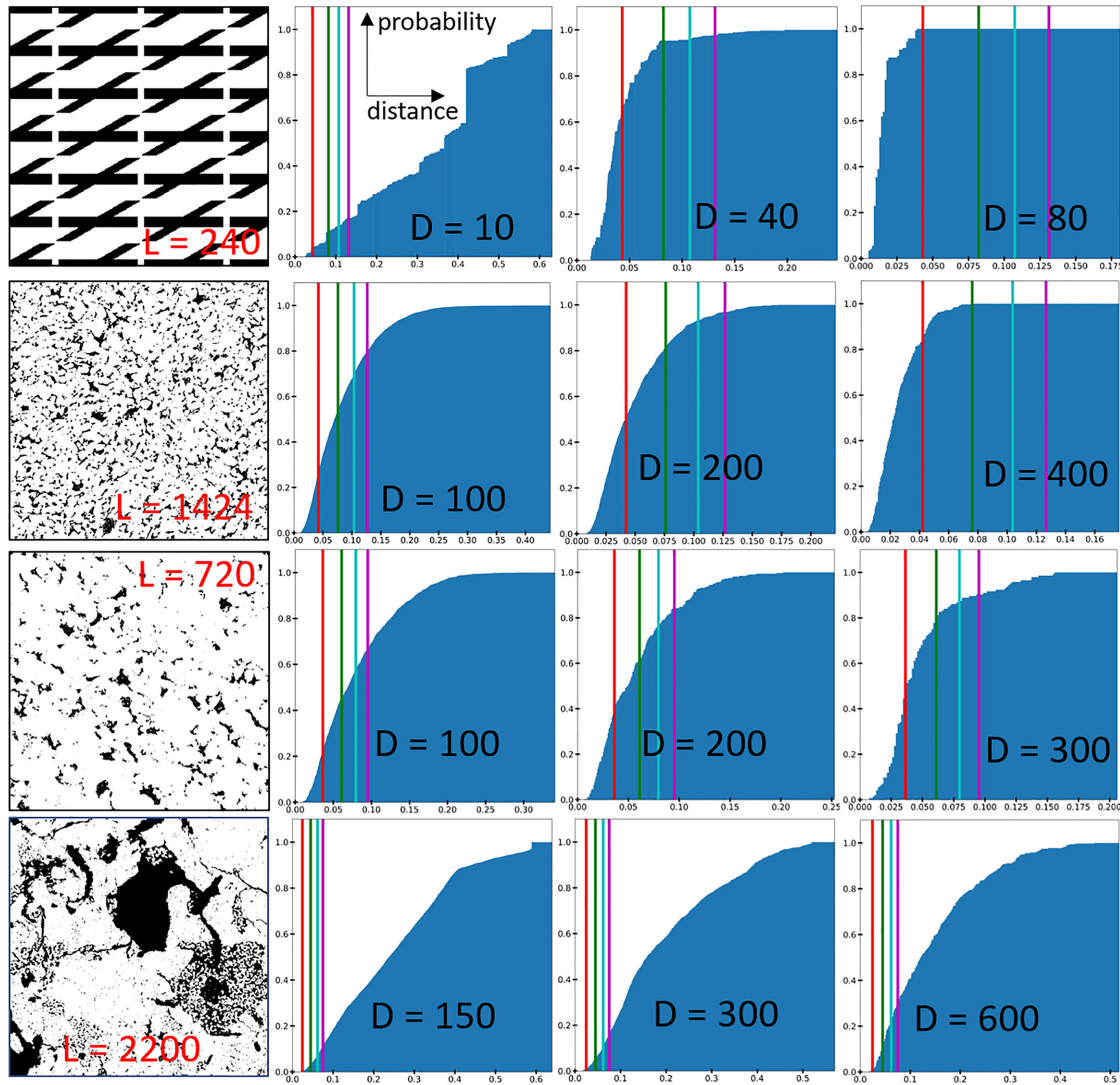
FIG. 6. The examples of binary 2D images and their corresponding distance distributions according to Eq. (8) as compared to the patch size D of the measuring window. On the distribution histogram, one can observe which patches fraction is covered by the distance value equal to one of the four thresholds according to Eq. (12) (threshold colors labels can be seen in Fig. 3). It can also be seen that for stationary structures the larger the patches size D is, the greater part of the distribution is covered by corresponding thresholds.

and, most importantly, noninfinite image size (something we discuss in more detail later). Nevertheless, the question is—where are the thresholds in terms of structural distances between strictly, weakly, and nonstationary structures?

We propose the thresholds in Eq. (12) to be the average differences between neighboring slices as shown in Fig. 3. This way, any sampling approach with $D >$ periodic unit cell will produce mean absolute difference [or $\frac{L_1}{n}$ distance according to Eq. (6)] between the patch's and the whole sample's correlation function descriptor distributions below T_1 (between nearest 1D slices computed along the same directions and with the same correlation length as for measuring windows) for such periodic structures (the upper case in Fig. 6). Weakly stationary structures, such as Poisson circles and some natural porous media samples, have the majority (e.g., >0.8) of their distance distribution below T_2. For carbonate samples, while the distances lie to the right of T_2, for $D \rightarrow \frac{L}{2}$ (where L is image's width) only a limited part of the distribution goes

beyond T_3. We speculate that the interface between T_2 and T_3 can be considered a transition zone and originate from the nonrepresentativeness of the image. In other words, carbonate samples could be found weakly stationary in case a larger image would be taken for the analysis under the condition that it would consist of the same structural features (i.e., with larger L, the Thresholds' values are not shifting to the right). The distribution spanning to the right of T_4 is a clear indicator of severe nonstationarity, as observed on Fig. 6 for the soil sample. Established in this manner, our thresholds are based on analysis of different images and physically consistent with stochastic processes, that could result in such images (artificial crosses and Poisson circles, or real images of porous media for which statistical process is hard to be identified).

As observed from Fig. 6, the size of the measuring window D affects the analysis results based on distance distribution. If D is too small to sample some representative part of the structure, then the distribution will fall out of T_{1-2}. The tail

of the distribution being in the T_3 transition zone can mean that the image size is close to the representative one. Sampling a larger part of the structure can lead to converging to (weak) stationarity. This is quite possible that carbonate samples from Fig. 5 show precisely this type of behavior, but only under a condition that structure outside the imaged region does not have statistically different features from those already present on the image. In such a case, increasing the size of the image will gradually move the distance distribution to the left and reach strict stationarity in the limit of the infinite image size. This logic is pretty much in line with conventional theory for infinitely large structures [5–7]. To demonstrate the influence of image size we applied the analysis to five Poisson disk images of the same spatial resolution but increasing size (up to 8×10^3 pixels in width). The results confirmed that the methodology is robust and shows stationarity for the same $D = 600$ pixels (see Supplemental Material [59]). However, while Thresholds were stable for these images, the distance distributions gradually moved to the left with increased size, that suggests that for infinite size image the stationarity will convert from the weak to the strict state. However, real structures for natural porous media are not periodic or infinite—there is always a possibility that the genesis of the material will render finding a stationary area impossible.

Clustering of patches based on CFs differences allows partitioning structure images into similar subregions (shown with different colors on Fig. 7). Variation in D leads to feature extraction with different resolutions and in the limit of D going to a pixel size is similar to the image segmentation procedure [64,65]. This means that our spatial analysis potentially allows automatic partitioning into stationary and nonstationary zones in addition to saying whether the image is stationary or not. The morphological REV based on CFs and the half of the image size can serve as logical lower and upper bounds on D. Extension of the methodology to provide such automated analysis will be the focus of our future work.

From Fig. 7, one can immediately observe that CFs-based analysis of heterogeneity closely resembles porosity variations (especially for small D). Porosity analysis in the form of coarseness [5] or local porosity [66] is a beneficial approach that led to uncovering hyper-uniformity [67] and local porosity-permeability relationships. However, porosity (or S_1) alone is not enough to characterize stationarity, as is evident from our simplified synthetic example with four quadrants on Fig. 8. Structures with the same porosity may possess very different structural features far from stationarity. In search for representativeness, porosity, surface area, or topological characteristics such as Minkowski functionals were previously used [68–71], which would not distinguish all quadrants (all four quadrants for porosity, two and four for other spatial averaged metrics) from each other. The same is true for spatially averaged CFs. Thus, analysis based on S_1, spatially averaged CFs and the one based on directional $S_2 + L_2$ produce different results. The immediate question is if it is enough to utilize directional $S_2 + L_2$ to analyze stationarity on images? While we believe the results presented in this work (see Fig. 5) to be robust as applied to the samples of porous media considered, one needs to account for the information con-
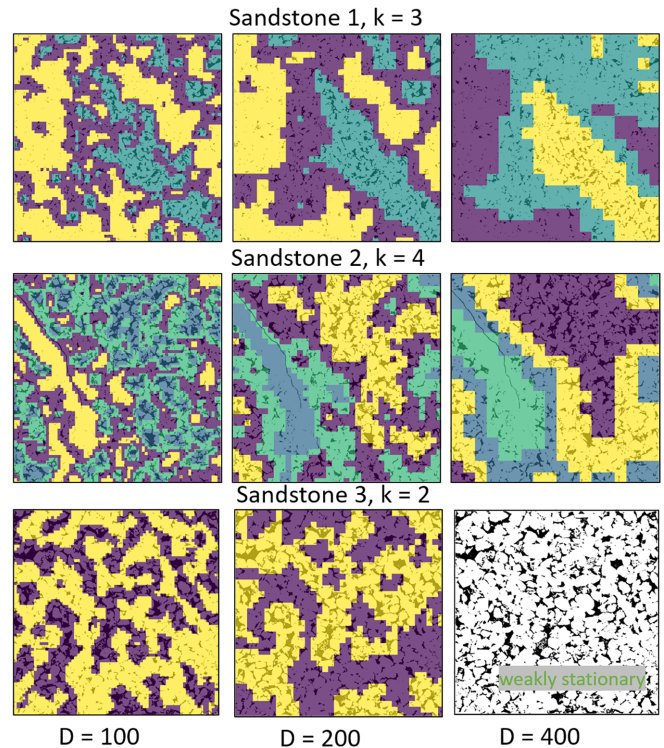

FIG. 7. The segmentation of the image into similar subregions based on correlation functions vector representation in Eq. (4) and K-Means clustering for different patches size D {100, 200, 400}. The subpatches within each subregion are colored similarly. Coloring is missing for image that were found to be homogeneous. This figure shows in dynamics how the assessment of homogeneity and the shape of homogeneous subregions change depending on the patches size D.

tent of correlation functions utilized for the analysis [9,10]. Most importantly, this means that while any CFs can be used to conclude that structure under study is nonstationary, the opposite is not true unless the used set of CFs possesses close to 100% information content. The indirect evidence that stationarity results are robust as shown in this work is that theoretically stationary structures such as crosses and Poisson disks were indeed found to be statistically homogeneous. Unfortunately, at the moment, the methodology to assess information content exists only for spatially averaged S_2 correlation function [9,10]; thus, it is of practical importance to incorporate the majority of existing CFs into the stationarity analysis.

Stationarity analysis is necessary to characterize structures and access their physical properties, as nonstationarity will compromise the homogenization and evaluation of effective macroscopic property [3,15,18,36,49,72,73] or comparison of materials morphology [74]. In the same fashion, it is invaluable for feature extraction for structure compression or machine learning [74–77], rigorous bounds [5], and effective medium approximations [78–81] for fast property estimation. In the context of measurements, stationarity is closely connected to representativeness [82,83], as measurements within the nonrepresentative volume will depend on the location. While in some cases nonrepresentativeness may result from
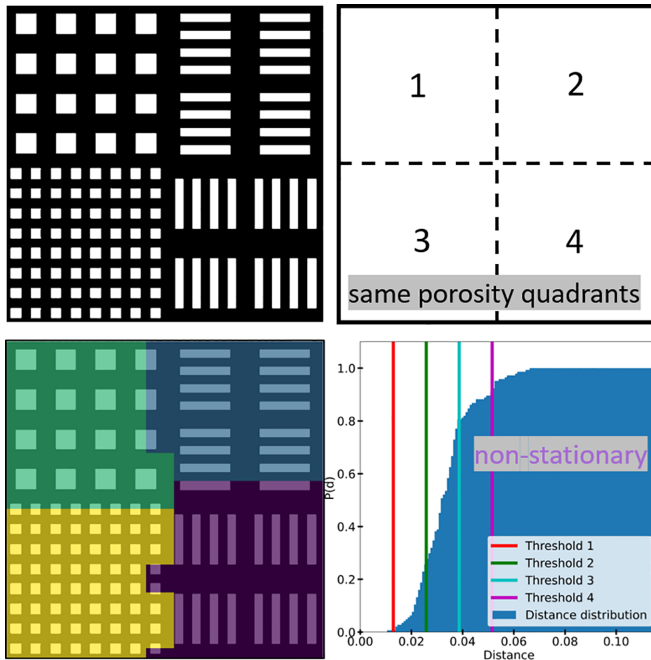
FIG. 8. Synthetic example of the structure with four quadrants having the same porosity distribution, some quadrants also have similar surface area and topology. Unlike conventional approaches, our methodology based on directional CFs correctly identifies all four structural types.

insufficient sample size and lead to a transition to nonstationarity (Fig. 3), huge distances between clusters based on computed CFs differences (see Fig. 6) may suggest that increasing the image size will not help—in other words, the structure at hand is essentially nonstationary. Stationarity quantification is necessary for input data for stochastic reconstructions [49,50], especially then averaged correlation are used [5,9–11,14,29,33,35–37,39–46,48–50,57,58,63,84]. It was shown that periodic structures (i.e., strictly stationary) could be reconstructed exactly [84]. Based on current findings, we hypothesize that for weakly stationary structures with high information content CFs, one can create reconstructions with the same physical properties; however exact reconstructions are not possible without full correlation map. We envision that for nonstationary media, accurate reconstructions [23] can be performed by partitioning into stationary and nonstationary regions with annealing accounting for local and global CFs. Our results also indicate that it is possible to measure nonstationarity experimentally by changing the field-of-view, e.g., by varying the beam size for small-angle scattering measurements [51]. Moreover, such measurements can be effectively combined with nonstationary stochastic reconstruction to recover structural images.

Each step above in Sec. II has building components that can be replaced or augmented (thus, leaving a room for future improvements). The list of these components and potential improvements include:

(1) *Spatial 2D patches grid creation method*—any method for creating a grid is potentially suitable. We chose a rectangular grid because it is a natural extension of digital pixelized and voxelized images and easy to implement. We allow patches to overlap to get smoother clustering results.

(2) *Structural descriptors*—we use specific correlation functions (S_2, L_2) as features representation vectors, because they have relatively high information content, and at the same time can be independently calculated along any direction. An important feature of the correlation functions that we used is the ability to compute it for patches of different sizes and map such patches in the same vector space. Any other functions with such properties are suitable for our algorithm. It is possible to extend the number of CFs to include surface functions [62,85], higher-order functions (e.g., three-point probability or surface functions) [86,87], or even vectorized topological metrics [88]. It is also important to note, that it is possible to use squared $\mathcal{L}_2$-metric instead of Eq. (6) (linearity is the only condition, therefore, the squared $\mathcal{L}_2$ and not just plain $\mathcal{L}_2$ is necessary). However, we chose $\mathcal{L}_1$-metric [89] for our homogeneity criteria and threshold evaluation because it is more robust to outliers.

(3) *Clustering*—any clustering algorithm which uses information about the distances between points and provides spherical clusters is suitable (for example, DBSCAN, cannot be used because it provides no guarantee about the form of the resulting clusters). We chose classical K-means because it fits well into the logic of the problem.

(4) *(In)homogeneity quantification*—to assess homogeneity, we use two independent criteria. The first criterion is calculated based on the distribution of $\mathcal{L}_1$ distances between the entire image and a whole set of 2D image patches. It has a natural interpretation: if the image is not homogeneous, then a sufficiently large proportion of individual image patches lies far enough from the whole "averaged" image in vector representation space. The second criterion is established on the basis of pairwise $\mathcal{L}_1$ distances between cluster centers and has a simple interpretation: To consider the observed clustering to be significant, it is necessary that the selected clusters are far enough from each other. Thus, these criteria require some thresholds as parameters. It may be possible to explore some other approaches to compute distances, however, our implementation is robust in this regard.

(5) *Establishing thresholds*—we used thresholds that are calculated in the unsupervised manner from the distribution of distances between descriptors of 1D patches (or slices) of the original image. Our goal in this work is to propose an approach that does not require any additional data to assess homogeneity, except for the input image itself, and at the same time has clear physical interpretation. The main advantage of the proposed method is the absence of the need for any labeled data or *a priori* statistical assumptions. We also understand that the proposed heuristic has a number of disadvantages: it may not be universal, it may not be suitable for images with radically different resolutions.

At the same time, it should be noted that thresholds for the conditions $\mathbb{H}_{homo}$ in Eq. (9) and $\mathbb{H}_{clusters}$ in Eq. (10) can be selected using different heuristics. There is a lot of room for research here. It must also be said that we have chosen the value of an $\alpha = 0.8$ experimentally, and it is probably possible to propose a more reasonable procedure for determining this parameter. We are planning to explore some of these possibilities to improve the methodology while developing

and applying (in)homogeneity analysis to experimental 3D images.

IV. CONCLUSION

In summary, we have presented a method to quantify the stationarity of structures from their images. By using (directional) correlation functions with sufficient information content and clusterization of subregions according to their differences in terms of these CFs, it is possible not only to assess stationarity of the whole image but also to automatically partition the image into stationary and nonstationary zones with variable resolution (however, this will require an extension of the methodology demonstrated in this study). With the help of the stationarity assessment technique, we were able to identify strictly and weakly stationary structure types and show that natural materials without periodic structural unit cells are never strictly stationary. The problem of scale can also affect the choice of parameters for (in)homogeneity analysis and, thus, requires automation as was mentioned above. We believe the methodology proposed in this paper will find its way into numerous research areas dealing with materials, structures, and measurements and modeling within such structures.

While here we focused on 2D binary (two-phase) structures, our approach is applicable to the analysis of general multiphase 3D structures—correlation and cross-correlation functions can be computed for any number of phases, or covariances can be used for continuous fields. To evaluate thresholds, neighboring 2D slices through 3D images instead of 1D slices can be used. With additional effort, our methodology can be extended for automatic analysis of images to extract homogeneous regions readily available for separate analysis of physical properties modeling. While such analysis for large 3D datasets is currently hampered by high computational expenses, using fast convolutions on modern GPU architectures (e.g., computation of full S_2, and possibly other CFs, maps) [85] can make the stationarity analysis highly applicable for data of any complexity. The usage of the proposed methodology is not limited to images of porous media necessary for pore-scale computations or Earth sciences in general. It can be effectively applied to a broad spectrum of structures ranging from cosmology and engineering to material sciences and biology.

ACKNOWLEDGMENTS

[1] V. Springel, C. S. Frenk, and S. D. White, The large-scale structure of the universe, Nature (London) **440**, 1137 (2006).

[2] F. Vazza and A. Feletti, The quantitative comparison between the neuronal network and the cosmic web, Front. Phys. **8**, 525731 (2020).

[3] S. Kelly, H. El-Sobky, C. Torres-Verdín, and M. T. Balhoff, Assessing the utility of FIB-SEM images for shale digital rock physics, Adv. Water Resour. **95**, 302 (2016).

[4] K. M. Gerke, E. V. Korostilev, K. A. Romanenko, and M. V. Karsanina, Going submicron in the precise analysis of soil structure: A FIB-SEM imaging study at nanoscale, Geoderma **383**, 114739 (2021).

[5] S. Torquato and H. Haslach Jr, Random heterogeneous materials: Microstructure and macroscopic properties, Appl. Mech. Rev. **55**, B62 (2002).

[6] M. Sahimi, *Heterogeneous Materials: Nonlinear and Breakdown Properties and Atomistic Modeling* (Springer, Berlin, 2003), Vol. 2.

[7] P. Adler, *Porous Media: Geometry and Transports* (Butterworth, Oxford, UK, 1992).

[8] L. Feigin, D. I. Svergun *et al.*, *Structure Analysis by Small-angle X-ray and Neutron Scattering* (Springer, Berlin, 1987), Vol. 1.

[9] C. J. Gommes, Y. Jiao, and S. Torquato, Density of states for a specified correlation function and the energy landscape, Phys. Rev. Lett. **108**, 080601 (2012).

[10] C. J. Gommes, Y. Jiao, and S. Torquato, Microstructural degeneracy associated with a two-point correlation function and its information content, Phys. Rev. E **85**, 051140 (2012).

[11] D. T. Fullwood, S. R. Niezgoda, and S. R. Kalidindi, Microstructure reconstructions from 2-point statistics using phase-recovery algorithms, Acta Mater. **56**, 942 (2008).

[12] G. Allaire, Homogenization and two-scale convergence, SIAM J. Math. Anal. **23**, 1482 (1992).

[13] V. V. Jikov, S. M. Kozlov, and O. A. Oleinik, *Homogenization of Differential Operators and Integral Functionals* (Springer Science & Business Media, Berlin, 2012).

[14] K. M. Gerke, M. V. Karsanina, and R. Katsman, Calculation of tensorial flow properties on pore level: Exploring the influence of boundary conditions on the permeability of three-dimensional stochastic reconstructions, Phys. Rev. E **100**, 053312 (2019).

[15] K. M. Gerke and M. V. Karsanina, How pore structure nonstationarity compromises flow properties representativity (REV) for soil samples: Pore-scale modelling and stationarity analysis, Eur. J. Soil Sci. **72**, 527 (2021).

[16] K. S. Lackner, A guide to CO2 sequestration, Science **300**, 1677 (2003).

[17] M. E. Boot-Handford, J. C. Abanades, E. J. Anthony, M. J. Blunt, S. Brandani, N. Mac Dowell, J. R. Fernández, M.-C. Ferrari, R. Gross, J. P. Hallett *et al.*, Carbon capture and storage update, Energy Environ. Sci. **7**, 130 (2014).

[18] Y. Kuzyakov and B. S. Razavi, Rhizosphere size and shape: Temporal dynamics and spatial stationarity, Soil Biol. Biochem. **135**, 343 (2019).

[19] M. J. Blunt, *Multiphase Flow in Permeable Media: A Pore-scale Perspective* (Cambridge University Press, Cambridge, UK, 2017).

[20] T. Gomi, R. C. Sidle, and J. S. Richardson, Understanding processes and downstream linkages of headwater systems: headwaters differ from downstream reaches by their close coupling to hillslope processes, more temporal and spatial variation, and their need for different means of protection from land use, BioScience **52**, 905 (2002).

[21] K. M. Gerke, R. C. Sidle, and D. Mallants, Preferential flow mechanisms identified from staining experiments in forested hillslopes, Hydrol. Process. **29**, 4562 (2015).

[22] D. Mallants and N. Chapman, How much does corrosion of nuclear waste matrices matter, Nat. Mater. **19**, 959 (2020).

[23] M. V. Karsanina and K. M. Gerke, Stochastic (re) constructions of nonstationary material structures: Using ensemble averaged correlation functions and nonuniform phase distributions, Physica A **611**, 128417 (2023).

[24] V. Cnudde and M. N. Boone, High-resolution x-ray computed tomography in geosciences: A review of the current technology and applications, Earth-Sci. Rev. **123**, 1 (2013).

[25] T. Bultreys, W. De Boever, and V. Cnudde, Imaging and image-based fluid transport modeling at the pore scale in geological materials: A practical introduction to the current state-of-the-art, Earth-Sci. Rev. **155**, 93 (2016).

[26] N. Lubbers, T. Lookman, and K. Barros, Inferring low-dimensional microstructure representations using convolutional neural networks, Phys. Rev. E **96**, 052111 (2017).

[27] P.-E. Chen, W. Xu, N. Chawla, Y. Ren, and Y. Jiao, Hierarchical n-point polytope functions for quantitative representation of complex heterogeneous materials and microstructural evolution, Acta Mater. **179**, 317 (2019).

[28] A. Cecen, Y. C. Yabansu, and S. R. Kalidindi, A new framework for rotationally invariant two-point spatial correlations in microstructure datasets, Acta Mater. **158**, 53 (2018).

[29] Y. Xu, S. Chen, P.-E. Chen, W. Xu, and Y. Jiao, Microstructure and mechanical properties of hyperuniform heterogeneous materials, Phys. Rev. E **96**, 043301 (2017).

[30] E. Ford, K. Maneparambil, S. Rajan, and N. Neithalath, Machine learning-based accelerated property prediction of two-phase materials using microstructural descriptors and finite element analysis, Comput. Mater. Sci. **191**, 110328 (2021).

[31] S. J. Semnani and R. I. Borja, Quantifying the heterogeneity of shale through statistical combination of imaging across scales, Acta Geotechnica **12**, 1193 (2017).

[32] P. Dimitriadis, K. Tzouka, D. Koutsoyiannis, H. Tyralis, A. Kalamioti, E. Lerias, and P. Voudouris, Stochastic investigation of long-term persistence in two-dimensional images of rocks, Spatial Statistics **29**, 177 (2019).

[33] Q. Sun, N. Zhang, M. Fadlelmula, and Y. Wang, Structural regeneration of fracture-vug network in naturally fractured vuggy reservoirs, J. Petrol. Sci. Eng. **165**, 28 (2018).

[34] E. Sevostianova, B. Leinauer, and I. Sevostianov, Quantitative characterization of the microstructure of a porous material in the context of tortuosity, Int. J. Eng. Sci. **48**, 1693 (2010).

[35] K. Gerke, M. Karsanina, and E. Skvortsova, Description and reconstruction of the soil pore space using correlation functions, Eurasian Soil Sc. **45**, 861 (2012).

[36] A. Derossi, K. M. Gerke, M. V. Karsanina, B. Nicolai, P. Verboven, and C. Severini, Mimicking 3d food microstructure using limited statistical information from 2D cross-sectional image, J. Food Eng. **241**, 116 (2019).

[37] H. Li, S. Singh, N. Chawla, and Y. Jiao, Direct extraction of spatial correlation functions from limited x-ray tomography data for microstructural quantification, Mater. Charact. **140**, 265 (2018).

[38] G. Barrall, L. Frydman, and G. Chingas, NMR diffraction and spatial statistics of stationary systems, Science **255**, 714 (1992).

[39] C. J. Gommes, Stochastic models of disordered mesoporous materials for small-angle scattering analysis and more, Microporous Mesoporous Mater. **257**, 62 (2018).

[40] P. Adler, C. G. Jacquin, and J. Quiblier, Flow in simulated porous media, Int. J. Multiphase Flow **16**, 691 (1990).

[41] C. L. Y. Yeong and S. Torquato, Reconstructing random media, Phys. Rev. E **57**, 495 (1998).

[42] J.-F. Thovert and P. M. Adler, Grain reconstruction of porous media: Application to a Bentheim sandstone, Phys. Rev. E **83**, 056116 (2011).

[43] M. V. Karsanina and K. M. Gerke, Hierarchical optimization: Fast and robust multiscale stochastic reconstructions with rescaled correlation functions, Phys. Rev. Lett. **121**, 265501 (2018).

[44] M. V. Karsanina, K. M. Gerke, E. B. Skvortsova, A. L. Ivanov, and D. Mallants, Enhancing image resolution of soils by stochastic multiscale image fusion, Geoderma **314**, 138 (2018).

[45] X. Li, Q. Teng, Y. Zhang, S. Xiong, and J. Feng, Three-dimensional multiscale fusion for porous media on microtomography images of different resolutions, Phys. Rev. E **101**, 053308 (2020).

[46] Y. Wu, P. Tahmasebi, C. Lin, L. Ren, and C. Dong, Multiscale modeling of shale samples based on low-and high-resolution images, Marine and Petroleum Geology **109**, 9 (2019).

[47] Y. Jiao, F. H. Stillinger, and S. Torquato, Modeling heterogeneous materials via two-point correlation functions: Basic principles, Phys. Rev. E **76**, 031110 (2007).

[48] K. M. Gerke and M. V. Karsanina, Improving stochastic reconstructions by weighting correlation functions in an objective function, Europhys. Lett. **111**, 56002 (2015).

[49] M. V. Karsanina, K. M. Gerke, E. B. Skvortsova, and D. Mallants, Universal spatial correlation functions for describing and reconstructing soil microstructure, PLoS ONE **10**, e0126515 (2015).

[50] P. Tahmasebi and M. Sahimi, Reconstruction of nonstationary disordered materials and media: Watershed transform and cross-correlation function, Phys. Rev. E **91**, 032401 (2015).

[51] C. J. Gommes, Small-angle scattering and scale-dependent heterogeneity, J. Appl. Crystallogr. **49**, 1162 (2016).

[52] K. M. Gerke, M. V. Karsanina, and D. Mallants, Universal stochastic multiscale image fusion: An example application for shale rock, Sci. Rep. **5**, 15880 (2015).

[53] C. Lantuejoul, Ergodicity and integral range, J. Microsc. **161**, 387 (1991).

[54] A. Moctezuma-Berthier, O. Vizika, and P. Adler, Macroscopic conductivity of vugular porous media, Transp. Porous Media **49**, 313 (2002).

[55] J. D. Hyman and C. L. Winter, Stochastic generation of explicit pore structures by thresholding Gaussian random fields, J. Comput. Phys. **277**, 16 (2014).

[56] C. J. Gommes and J.-P. Pirard, Morphological models of complex ordered materials based on inhomogeneously clipped Gaussian fields, Phys. Rev. E **80**, 061401 (2009).

[57] Y. Jiao and N. Chawla, Modeling and characterizing anisotropic inclusion orientation in heterogeneous material via directional cluster functions and stochastic microstructure reconstruction, J. Appl. Phys. **115**, 093511 (2014).

[58] K. M. Gerke, M. V. Karsanina, R. V. Vasilyev, and D. Mallants, Improving pattern reconstruction using directional correlation functions, Europhys. Lett. **106**, 66002 (2014).

[59] See Supplemental Material at http://link.aps.org/supplemental/10.1103/PhysRevE.108.064128 for additional cases of (in)homogeneity assessment and results for large Poisson disk images.

[60] M. A. Knackstedt, A. P. Sheppard, and M. Sahimi, Pore network modelling of two-phase flow in porous rock: The effect of correlated heterogeneity, Adv. Water Resour. **24**, 257 (2001).

[61] R. Ledesma-Alonso, R. Barbosa, and J. Ortegón, Effect of the image resolution on the statistical descriptors of heterogeneous media, Phys. Rev. E **97**, 023304 (2018).

[62] Z. Ma and S. Torquato, Precise algorithms to compute surface correlation functions of two-phase heterogeneous media and their applications, Phys. Rev. E **98**, 013307 (2018).

[63] E. V. Lavrukhin, K. M. Gerke, K. A. Romanenko, K. N. Abrosimov, and M. V. Karsanina, Assessing the fidelity of neural network-based segmentation of soil XCT images based on pore-scale modelling of saturated flow properties, Soil Till. Res. **209**, 104942 (2021).

[64] A. Lucchi, K. Smith, R. Achanta, G. Knott, and P. Fua, Supervoxel-based segmentation of mitochondria in EM image stacks with learned shape features, IEEE Trans. Med. Imag. **31**, 474 (2011).

[65] D. Hu, P. Ronhovde, and Z. Nussinov, Replica inference approach to unsupervised multiscale image segmentation, Phys. Rev. E **85**, 016101 (2012).

[66] R. Hilfer, Local-porosity theory for flow in porous media, Phys. Rev. B **45**, 7115 (1992).

[67] S. Torquato and F. H. Stillinger, Local density fluctuations, hyperuniformity, and order metrics, Phys. Rev. E **68**, 041113 (2003).

[68] D. Zhang, R. Zhang, S. Chen, and W. E. Soll, Pore scale study of flow in porous media: Scale dependency, REV, and statistical REV, Geophys. Res. Lett. **27**, 1195 (2000).

[69] R. Al-Raoush and A. Papadopoulos, Representative elementary volume analysis of porous media using x-ray computed tomography, Powder Technol. **200**, 69 (2010).

[70] H.-J. Vogel, U. Weller, and S. Schlüter, Quantification of soil structure based on Minkowski functions, Comput. Geosci. **36**, 1236 (2010).

[71] M. S. Costanza-Robinson, B. D. Estabrook, and D. F. Fouhey, Representative elementary volume estimation for porosity, moisture saturation, and air-water interfacial areas in unsaturated porous media: Data quality implications, Water Resour. Res. **47**, W07513 (2011).

[72] T. Khachkova, V. Lisitsa, G. Reshetova, and V. Tcheverda, GPU-based algorithm for evaluating the electrical resistivity of digital rocks, Comput. Math. Appl. **82**, 200 (2021).

[73] N. M. Evstigneev, O. I. Ryabkov, and K. M. Gerke, Stationary stokes solver for single-phase flow in porous media: A blastingly fast solution based on algebraic multigrid method using GPU, Adv. Water Resour. **171**, 104340 (2023).

[74] M. V. Karsanina, E. V. Lavrukhin, D. S. Fomin, A. V. Yudina, K. N. Abrosimov, and K. M. Gerke, Compressing soil structural information into parameterized correlation functions, Eur. J. Soil Sci. **72**, 561 (2021).

[75] J. Havelka, A. Kučerová, and J. Sýkora, Compression and reconstruction of random microstructures using accelerated lineal path function, Comput. Mater. Sci. **122**, 102 (2016).

[76] M. Röding, Z. Ma, and S. Torquato, Predicting permeability via statistical learning on higher-order microstructural information, Sci. Rep. **10**, 15239 (2020).

[77] S. Kamrava, P. Tahmasebi, and M. Sahimi, Linking morphology of porous media to their macroscopic permeability by deep learning, Transp. Porous Media **131**, 427 (2020).

[78] J. D. Eshelby, The determination of the elastic field of an ellipsoidal inclusion, and related problems, Proc. R. Soc. London A **241**, 376 (1957).

[79] T. Mori and K. Tanaka, Average stress in matrix and average elastic energy of materials with misfitting inclusions, Acta Metall. **21**, 571 (1973).

[80] I. O. Bayuk, M. Ammerman, and E. M. Chesnokov, Elastic moduli of anisotropic clay, Geophysics **72**, D107 (2007).

[81] A. G. Hunt and M. Sahimi, Flow, transport, and reaction in porous media: Percolation scaling, critical-path analysis, and effective medium approximation, Rev. Geophys. **55**, 993 (2017).

[82] S. R. Niezgoda, D. M. Turner, D. T. Fullwood, and S. R. Kalidindi, Optimized structure based representative volume element sets reflecting the ensemble-averaged 2-point statistics, Acta Mater. **58**, 4432 (2010).

[83] J. Zeman and M. Šejnoha, From random microstructures to representative volume elements, Modell. Simul. Mater. Sci. Eng. **15**, S325 (2007).

[84] M. G. Rozman and M. Utz, Uniqueness of reconstruction of multiphase morphologies from two-point correlation functions, Phys. Rev. Lett. **89**, 135501 (2002).

[85] A. Samarin, V. Postnicov, M. V. Karsanina, E. V. Lavrukhin, D. Gafurova, N. M. Evstigneev, A. Khlyupin, and K. M. Gerke, Robust surface-correlation-function evaluation from experimental discrete digital images, Phys. Rev. E **107**, 065306 (2023).

[86] H. Malmir, M. Sahimi, and Y. Jiao, Higher-order correlation functions in disordered media: Computational algorithms and application to two-phase heterogeneous materials, Phys. Rev. E **98**, 063317 (2018).

[87] V. Postnicov, M. V. Karsanina, A. Khlyupin, and K. M. Gerke, The 2- and 3-point surface correlation functions calculations: From novel exact continuous approach to improving methodology for discrete images, Physica A **628**, 129137 (2023).

[88] A. S. Zubov, D. A. Murygin, and K. M. Gerke, Pore-network extraction using discrete morse theory: Preserving the topology of the pore space, Phys. Rev. E **106**, 055304 (2022).

[89] V. Sundararaghavan, M. N. Shah, and J. P. Simmons, Methodology for estimation of intrinsic dimensions and state variables of microstructures, Phys. Rev. E **108**, 035001 (2023).

[90] www.porenetwork.com.